Influence of the ion charge state on emission energies of Auger electrons exemplified in Ar and Xe clusters

Niklas Golchert [1,*] Eetu Pelimanni [2] Nils Kiefer [1] Lutz Marder [1] Catmarna Küstner-Wetekam [1] Christina Zindel [1] Yusaku Terao [1] Emilia Heikura [1] Madhusree Roy Chowdhury [1] Adrian Krone [1] Arne Schröder [1] Maria Novella Piancastelli [3] Tatiana Marchenko [3,4] Iyas Ismail [3,4] Oksana Travnikova [3,4] Ralph Püttner [5] Antti Kivimäki [6] Kirill Chernenko [6] Denis Céolin [4] Olle Björneholm [7] Marc Simon [3,4] Arno Ehresmann [1] Minna Patanen [2] and Andreas Hans [1,†]

[1]*Institut für Physik und CINSaT, Universität Kassel, Heinrich-Plett-Straße 40, D-34132 Kassel, Germany*
[2]*Nano and Molecular Systems Research Unit, Faculty of Science, University of Oulu, Oulu 90014, Finland*
[3]*Sorbonne Université, CNRS, UMR 7614, Laboratoire de Chimie Physique-Matière et Rayonnement, F-75005 Paris, France*
[4]*Synchrotron SOLEIL, l'Orme des Merisiers, Saint-Aubin, BP 48, F-91192 Gif-sur-Yvette Cedex, France*
[5]*Fachbereich Physik, Freie Universität Berlin, Arnimallee 14, D-14159 Berlin, Germany*
[6]*MAX IV Laboratory, Lund University, P.O. Box 118, SE-22100 Lund, Sweden*
[7]*Chemical and Biomolecular Physics, Department of Physics and Astronomy, Uppsala University, Box 516, 751 20 Uppsala, Sweden*

(Received 1 July 2025; accepted 9 March 2026; published 9 April 2026)

We report on the shift of energies released during Auger cascades in rare-gas ions, when the ions are not isolated but embedded in a homogeneous cluster. By combining high-resolution electron spectroscopy with multielectron coincidence spectroscopy of small Ar and Xe clusters, we investigate the dependence of Auger electron emission energies on the charge state of the emitting ion in the polarizable cluster medium up to charge states of +4. Our results show deviations from the predictions of the established electrostatic Born model by a factor of ≈2 for the final step of the cascades.

DOI: 10.1103/8g56-ghtb

I. INTRODUCTION

Understanding complex radiation-induced processes at the atomic level is an important aspect for fundamental atomic and cluster physics and corresponding applied scientific fields [1–3]. For experimentally probing fundamental processes occurring in dense media, rare-gas (RG) clusters serve as attractive prototype systems due to their inert behavior and a considerable amount of knowledge on their properties. Although the local electronic structure in rare-gas clusters is often considered to be atomiclike, the influence of the neighboring atoms on the energy levels [4–6] and relaxation mechanisms of the photoionized or photoexcited site is apparent (see Ref. [7] and references therein). The exact energies of orbitals are a decisive factor for the accessibility of relaxation processes (including nonlocal decay mechanisms) and for the determination of the amount of energy that is released during these processes. The origin of energy shifts of atomiclike orbitals in clusters with respect to those of atoms is twofold: (1) A delocalization of valence orbitals, resulting in a bandlike structure [8] and (2) the polarization of the surrounding atoms decreases the electrostatic potential energy of an embedded ion [9]. In a simplified classical electrostatic model, where the ion is assumed to be a sphere, charged with an integer multiple z times the elementary charge e, and of fixed radius r_i, that is surrounded by a continuous, isotropic, polarizable dielectric medium, the ion's solvation energy is approximated by the Born equation. For a single solvated ion, this translates to an energy shift ΔE_z in ground state (GS) binding energies with respect to the isolated ion. It is proportional to the square of the charge state z [9]:

$$\Delta E_z \propto -\frac{z^2}{r_i}. \tag{1}$$

Additional information on the Born model and the detailed derivation of Eq. (1) are provided in Appendix A. Despite its simplicity, the Born model allows to make good predictions with little computational costs and can be applied to several problems, e.g., free solvation energy determination of ions [10,11]. Although ions that are embedded in a rare-gas cluster are not the typical target of electrochemistry, the origin of the electrostatic energy difference is still the same. Therefore, by studying binding energy shifts in rare-gas clusters, insights about aspects of ion solvation as well as solvation models can be obtained. Other models that describe ion solvation can be divided into *implicit solvent models*, like the Born model, and *explicit solvent models*. While explicit solvent models can take molecular dynamics into account, they have high computational costs depending on the sampling size [12].

*Contact author: niklas.golchert@uni-kassel.de
†Contact author: hans@physik.uni-kassel.de

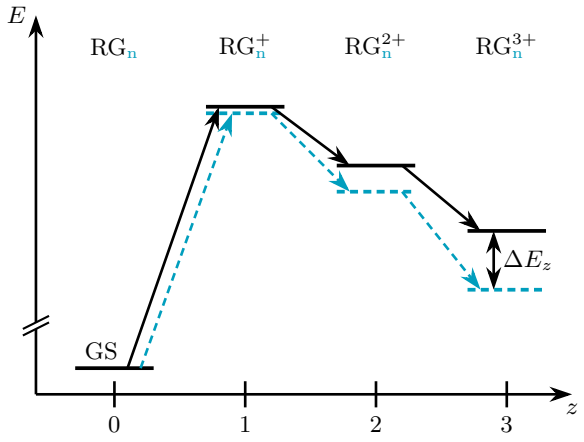

FIG. 1. Schematic illustration of the relative energies of selected states in a generic RG atom (*monomer*, black solid) and cluster (blue dashed) according to the Born equation (1). After core ionization from the electronic GS, the excited RG_n^{z+} ions decay via a multistep Auger cascade, during which the energy shift of the states in the cluster, relative to the atomic value, depends quadratically on the charge.

More complex implicit solvent models like the generalized Born model [13], the polarizable continuum model [14,15], the Poisson model [16–18], or the Poisson-Boltzmann model [12,19] treat the surrounding medium as a continuum, but they take additional deviations into account, which are not covered by the Born model. This includes, for example, treating (macro-) molecules as well as arbitrary shapes and charge distributions as the solute [13,14] or including the presence of counterions or electrolytes in the description of the solvent [12]. Other models divide the solvent surrounding the ion into a first solvation shell and a polarizable continuum beyond the first solvation shell [4,20]. From microscopic simulations, it was found that the polarization of the first solvation shell saturates for a certain ionic charge, which leads to a smaller, effective relative permittivity and, therefore, to smaller electrostatic energy differences compared to the isolated ion than predicted by the Born model [11]. While there is a manifold of more advanced models describing the solvation of ions, the mentioned extensions of the Born model, i.e., the implicit solvent models, do not give further insight for the case of rare-gas clusters beyond Eq. (1). Therefore, the dependence of the solvation energy on the ionic charge should correctly describe the relevant Auger electron kinetic energy shifts of the present study. We report, however, experimental results with significant deviations to the model, which may serve as benchmarks for further theoretical descriptions.

For the following discussions, we assume the radius r_i of a certain ion and the permittivity ε_r of the cluster to be constant.

The energy differences according to Eq. (1) are visualized in Fig. 1 for exemplary energy levels in differently charged ions of a generic RG atom and cluster. Such a scenario of a successively increasing charge of an ion is common during an autoionization cascade, e.g., initiated by inner-shell photoionization, for which in each autoionization step the charge of the ion increases by one elementary unit.

Experimentally, the direct observable is not the (absolute) energy of a specific state, but the energy difference between two states in a transition. Most prominently, the kinetic energy of an electron emitted in an Auger process corresponds to the energy difference of two levels in two ions differing by one elementary charge. The Auger process is exploited in various applications, for example, in radiotherapy [21], material characterization [22], as well as in the field of ultrafast electron and nuclear dynamics [1,23–25]. The quadratic dependence of the electron binding energy [Eq. (1)] shift on the ion's charge state results in a linear dependence of electron energies released during Auger decay from an initial state with charge z to a final state with charge $(z+1)$:

$$\begin{aligned}\Delta E^{\text{Auger}}_{(z)\to(z+1)} &= \Delta E_{z+1} - \Delta E_z = ((z+1)^2 - z^2))\Delta E_1 \\ &= (2z+1)\Delta E_1. \end{aligned} \tag{2}$$

Here, ΔE_1 is the shift observed for singly ionized atoms, i.e., $z = 1$. For a single-step Auger decay in rare-gas clusters, this relation is experimentally well quantified [26–28]. If an atom or a molecule, however, is exposed to radiation from state-of-the-art high-energetic or highly brilliant light sources, the population of multiply charged states can become dominant. This can proceed via sequential multiphoton absorption [29,30] and/or deep inner-shell ionization followed by a cascade of Auger processes [1,31–33].

Here, we report the first experimental observation of Auger cascades leading up to quadruply charged ions inside a cluster. For transitions in these cascades, we observe shifts of Auger electron kinetic energies that increase for each additional step in the cascade. For transitions where the $(2z+1)$ prediction from the Born model does not agree with the experimental results, we describe the deviations by shift factors defined as

$$k_{(z)\to(z+1)} = \Delta E^{\text{Auger}}_{(z)\to(z+1)}/\Delta E_1. \tag{3}$$

Experiments on Auger cascades face multiple challenges due to the high number of emitted electrons and their assignment to accessible channels. In principle, time-of-flight coincidence studies are capable of disentangling cascades of electron emission [34–36]. They are, however, inferior in energy resolution for electrons with relatively high kinetic energies. Therefore, we combined results from three independent experiments on homogeneous Ar and Xe clusters with two different types of electron spectrometers.

In the following, we shall consider the studied cascades that lead to Ar^{4+} and Xe^{4+} ions. As studied for Ar monomers, quadruply charged states are efficiently populated by 1*s* photoionization and three consecutive Auger decays [33]:

$$h\nu + \text{Ar} \to \text{Ar}^+(1s^{-1}) + e^-_{\text{photoelectron}}, \tag{4}$$

$$\text{Ar}^+(1s^{-1}) \to \text{Ar}^{2+}(2p^{-2}) + e^-_{KLL\,\text{Auger}}, \tag{5}$$

$$\text{Ar}^{2+}(2p^{-2}) \to \text{Ar}^{3+}(2p^{-1}3p^{-2}) + e^-_{LMM(1)\,\text{Auger}}, \tag{6}$$

$$\text{Ar}^{3+}(2p^{-1}3p^{-2}) \to \text{Ar}^{4+}(3p^{-4}) + e^-_{LMM(2)\,\text{Auger}}. \tag{7}$$

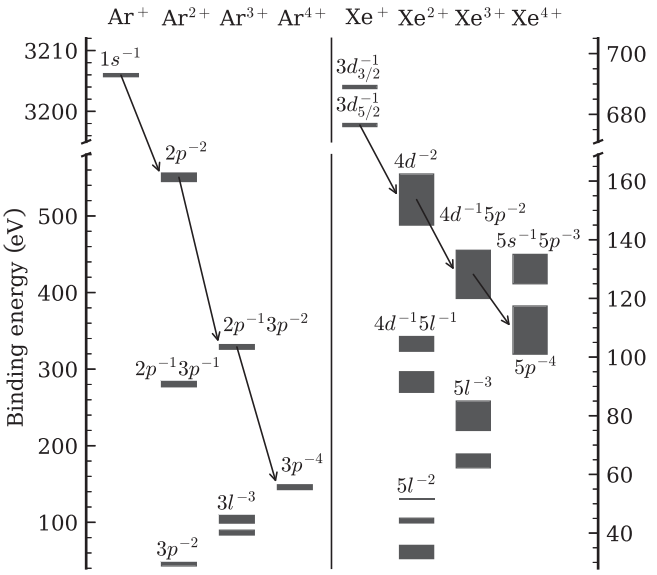

FIG. 2. Simplified energy level diagrams of Ar and Xe ions, containing the ionic states and transitions discussed in Eqs. (5)–(7) and (9)–(11).

In Xe, a similar cascade can be initiated by ionization of the $3d$ orbital [32]:

$$h\nu + \mathrm{Xe} \rightarrow \mathrm{Xe}^{+}(3d^{-1}) + e^{-}_{\text{photoelectron}}, \tag{8}$$

$$\mathrm{Xe}^{+}(3d^{-1}) \rightarrow \mathrm{Xe}^{2+}(4d^{-2}) + e^{-}_{MNN\ \text{Auger}}, \tag{9}$$

$$\mathrm{Xe}^{2+}(4d^{-2}) \rightarrow \mathrm{Xe}^{3+}(4d^{-1}5p^{-2}) + e^{-}_{NOO(1)\ \text{Auger}}, \tag{10}$$

$$\mathrm{Xe}^{3+}(4d^{-1}5p^{-2}) \rightarrow \mathrm{Xe}^{4+}(5p^{-4}) + e^{-}_{NOO(2)\ \text{Auger}}. \tag{11}$$

Both cascades are visualized in Fig. 2, where the binding energies of ionic states in Ar and Xe, as well as the Auger transitions outlined in Eqs. (5)–(7) and (9)–(11), are shown. These cascades are well investigated for atomic Ar and Xe [31–35]. Among the plethora of competing channels [31–33,35], we exclusively focus on the channels highlighted in Fig. 2 since they are dominant and also well defined by the kinetic energies of the emitted electrons. They therefore serve as good showcases for the cascade from neutral atoms to quadruply charged ions.

II. EXPERIMENTS

The experiments were performed in three independent campaigns (I–III). Two experiments (I and II) were performed on Ar clusters, both at the GALAXIES beamline [37] of the synchrotron SOLEIL, and one (III) on Xe clusters at the FinEstBeAMS beamline [38] at the synchrotron MAX IV.

Using the HAXPES endstation [39] for the first experiment (I), high-resolution electron spectra of Ar were obtained. The HAXPES endstation features a high-resolution Scienta EW4000 hemispherical electron analyzer (HEA). This instrument was used in combination with a rare-gas cluster source, with the cluster jet crossing the synchrotron beam at a 90° angle and pointing directly toward the opening of the HEA. Cluster formation happens when the gas expands supersonically from a high-pressure reservoir (8 bars) through a 5 mm long conical nozzle with 20 µm orifice and a full opening angle of 40°. By adjusting the nozzle position, only the center of the cluster jet passes the 300 µm opening of a skimmer that separates the expansion chamber from the interaction chamber and therefore reduces the amount of uncondensed monomers in the interaction region. Using empirical scaling laws for cluster size determination [40–42] with the gas-specific constants from Ref. [43], an average Ar cluster size of $\langle N \rangle = 20$ was determined. The photon energy was set to 3300 eV being well above the Ar $1s$ ionization threshold ($E_{\text{bin}} = 3206.3$ eV [44]). For the detected kinetic energy range 2655–2672 eV, a pass energy of 200 eV and a curved entrance slit of 0.8 mm were selected at the HEA. For the range 180–235 eV, these parameters were changed to a pass energy of 100 eV and a straight entrance slit of 1.5 mm. Both settings result in a kinetic energy resolution of about 400 meV. A large part of the kinetic energy range of the *LMM*(1) Auger electron [see Eq. (6)] of Ar is essentially free of other overlapping features, which is not the case for the kinetic energy range of the *LMM*(2) Auger electron [see Eq. (7)] [33]. It is therefore possible to obtain a clear and highly resolved spectrum of Auger decays up to triply charged states, but not further.

Consequently, we performed two further experiments (II and III) applying time-of-flight multielectron coincidence spectroscopy. This method allows to disentangle energetically overlapping features by using coincidence conditions. These experiments were conducted using a customized setup equipped with the same cluster source as in experiment I but combined with a 60 cm long magnetic-bottle-type time-of-flight electron spectrometer (MBES) [45]. The MBES is a spectrometer that collects electrons emitted from an interaction region with an angular acceptance of almost 4π sr by using a combination of a strong inhomogeneous magnetic field (≈0.5 T) close to the interaction region with a weak homogeneous magnetic field in a drift region [45,46]. The time of flight of the electrons is measured with respect to a start signal and converted into units of kinetic energy. The time-resolved measurement enables the coincident detection of electrons originating from the same process, if the time between consecutive excitation pulses is sufficiently long. By applying static voltages between the interaction region and the drift tube, electrons may be accelerated or decelerated either to detect very slow electrons or increase the resolution for fast electrons. A number of electrons detected within a selected time interval are referred to as being coincident and are stored in a format where the time of flight of these coincident electrons is sorted according to their arrival time, where an earlier arrival time directly corresponds to a higher electron kinetic energy. However, with the present experimental equipment, two electrons with very similar kinetic energies cannot be detected in coincidence with one another if their time-of-flight difference is below the detector dead time. Consequently, this leads to a distortion in the spectra of correlated electron-emitting processes that have similar emission energies. In the present work, this is relevant for the Xe *NOO*(1) and *NOO*(2) spectra.

Experiment II was again conducted at the GALAXIES beamline, using the single-bunch operation mode of SOLEIL.

TABLE I. Temporal order in which the electrons emitted during the pathways outlined in Eqs. (4)–(7) and (8)–(11) are detected with the MBES. An exciting photon energy of 3600 eV (688 eV) was used for the measurements on Ar (Xe).

	e_1^-	e_2^-	e_3^-	e_4^-
Ar:	*KLL*	Photoelectron	*LMM*(1)	*LMM*(2)
Xe:	*MNN*	*NOO*(1)	*NOO*(2)	Photoelectron

Now, the cascade after 1*s* ionization in Ar clusters ($\langle N\rangle = 13$ according to Ref. [41]) was investigated using the described coincidence technique. Here, an exciting photon energy of 3600 eV and a retardation potential of $U_{\mathrm{ret}} = -175$ V at the MBES were chosen. An experimental kinetic energy resolution of $(E_{\mathrm{kin}} + eU_{\mathrm{ret}})/\Delta E_{\mathrm{kin}} \approx 17$ was achieved for the relevant energy range 180–235 eV.

Experiment III was performed on Xe clusters at the FinEstBeAMS beamline [38] at the Swedish synchrotron MAX IV, operated in single-bunch mode. The cluster source conditions were set so that an average Xe cluster size of $\langle N\rangle = 30$ was produced according to Ref. [41]. Using a photon energy of 688 eV, core ionization of the $3d_{5/2}$ orbital ($E_{\mathrm{bin}} = 676.4$ eV [47]) in Xe is possible. A small retardation voltage of $U_{\mathrm{ret}} = -4$ V was applied at the MBES to enhance the resolution [$(E_{\mathrm{kin}} + eU_{\mathrm{ret}})/\Delta E_{\mathrm{kin}} \approx 30$] of the features relevant to this work. Note that in all experiments the cluster target contains uncondensed monomers. By detuning the nozzle from the skimmer, atomic reference spectra have been recorded. The expected temporal order of detection for the electrons emitted during the pathways outlined in Eqs. (4)– (7) and (8)–(11) is given in Table I.

III. RESULTS AND DISCUSSION

A. Ar clusters—high-resolution spectra

In this section, high-resolution Auger electron spectra of Ar monomers and clusters, measured above the 1*s* ionization threshold, are presented. In Figs. 3 and 4, the black solid lines depict the Auger electron spectrum of Ar monomers, while the gray filled areas, labeled *Total*, display the measured spectrum from a partially condensed jet. For the interpretation of the *Total* spectra, we use an approach to reproduce them by shifting the atomic spectra by respective values for cluster surface and bulk components [5]. The sums of the measured monomer and the modeled surface and bulk contributions (blue dotted lines, labeled *Total*) are then compared with the experimental *Total* spectra. The parameters for this modeling are derived from the relative intensities, shifts, and widths of cluster contributions in our experimental photoelectron spectra. Details on the analysis of the photoelectron spectra are given in Appendix B, with the results summarized in Fig. 10 and Table II. Briefly, the energy shifts of surface (S) and bulk (B) components are determined from the Ar 2*p* photoelectron spectrum ($\Delta E_{1,\mathrm{S}} = 0.66$ eV and $\Delta E_{1,\mathrm{B}} = 0.95$ eV). These values are assumed to be identical for the Ar 1*s* core hole (our first ionization step) and all other core holes in Ar [6]. As the escape probability of electrons from the bulk or from the surface of clusters depends on their kinetic

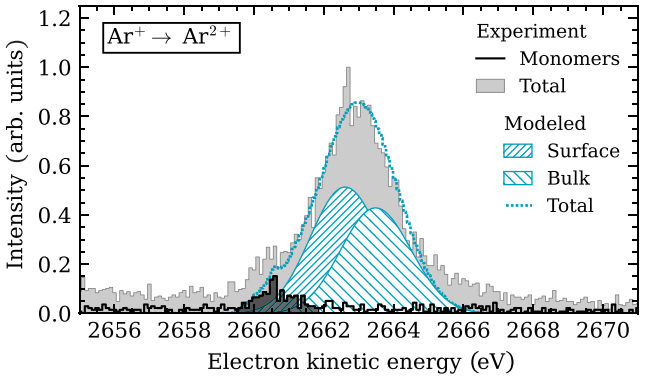

FIG. 3. High-resolution Ar $KL_{2,3}L_{2,3}$ Auger electron spectra [$Ar^+(1s^{-1}) \rightarrow Ar^{2+}(2p^{-2}\ ^1D_2)$] after 1*s*-electron photoionization at a photon energy of 3300 eV. The presented spectra are obtained from diffusive Ar gas (black, solid line) and from a partially condensed cluster jet (gray, filled area), the latter containing signal from Ar clusters and monomers alike. Additionally, modeled cluster contributions, consisting of surface and bulk, are depicted (blue, hatched areas). These are copies of the monomer spectrum in the range 2658.4–2662 eV (black, filled area), shifted by 1.98 eV (3×0.66 eV) for the surface component and 2.85 eV (3×0.95 eV) for the bulk component according to the Born model and convolved with Gaussians of 0.86 eV width, respectively (see main text for details). The blue dotted line shows the sum of the experimental *Monomer* and modeled *Surface* and *Bulk* contributions.

energy [48], their relative intensities in the two spectral ranges (180–235 eV for the *L*-shell decay and 2655–2672 eV for the $KL_{2,3}L_{2,3}$ Auger decay) differ. The same argument holds for the cluster-to-atom ratio. Therefore, the intensity ratios are taken from photoelectron spectra recorded at similar kinetic energies. For the low kinetic energy range, the cluster-to-atom and surface-to-bulk intensity ratios ($I_{\mathrm{C/A}} = 3.5$ and $I_{\mathrm{S/B}} = 2.1$) were determined from the 1*s* photoelectron spectrum measured at 3336 eV, resulting in photoelectron kinetic energies of about 130 eV. For the high kinetic energy range, intensity ratios of $I_{\mathrm{C/A}} = 16.7$ and $I_{\mathrm{S/B}} = 1.2$ are obtained from the 2*p* photoelectron spectrum recorded at 2920 eV, approximately 2670 eV above the 2*p* ionization threshold. In Fig. 3, the electron spectrum of Ar monomers and clusters in the range of the Ar $KL_{2,3}L_{2,3}$ Auger decay leading to the $Ar^{2+}(2p^{-2})\ ^1D_2$ state is displayed.

TABLE II. Results of the photoelectron fits. ΔE_1 denotes the binding energy difference between the monomer and the surface or bulk atom. $W_{\mathrm{A,S,B}}$ gives the Gaussian standard deviation of the atomic, surface, and bulk profiles. In the case of Voigt profiles, this corresponds solely to the Gaussian part of the profile. Finally, the intensity ratios $I_{\mathrm{S/B}}$ of surface-to-bulk and $I_{\mathrm{C/A}}$ of cluster-to-atom are shown.

	$\Delta E_{1,\mathrm{S}}$ (eV)	$\Delta E_{1,\mathrm{B}}$ (eV)	W_{A} (meV)	W_{B} (meV)	W_{S} (meV)	$I_{\mathrm{S/B}}$	$I_{\mathrm{C/A}}$
Ar 2*p*	0.66	0.95	159	179	179	1.2	16.7
Ar 1*s*	0.66	0.95	186	187	187	2.1	3.5
Xe 4*d*	0.73	1.02	201	263	263	3.7	4.3

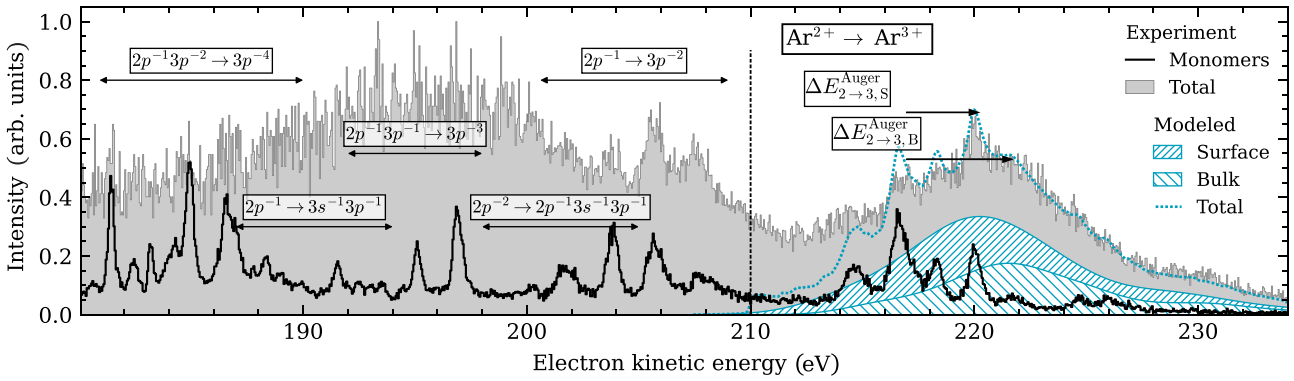

FIG. 4. High-resolution *LMM* Auger electron spectra measured at a photon energy above the Ar 1*s* ionization threshold. The spectra are obtained from diffusive Ar gas (black, solid line) and from a partially condensed cluster jet (gray, filled area), the latter containing signal from Ar clusters and monomers alike. The spectrum to the right of the vertical dotted line contains predominantly signal from the *LMM*(1) Auger decay [$Ar^{2+}(2p^{-2}) \rightarrow Ar^{3+}(2p^{-1}3p^{-2})$] with only minor contributions from other processes [33,35]. In the range 180–210 eV, further Auger channels associated with the Ar *L*-shell decay are shown in Refs. [33,35]. Additionally, modeled cluster contributions, consisting of surface and bulk, are depicted (blue, hatched areas). These are copies of the monomer spectrum in the range 210–234 eV, shifted by 3.3 eV (5×0.66 eV) for the surface component and 4.75 eV (5×0.95 eV) for the bulk component according to the Born model and convolved with Gaussians of 2.0 and 1.5 eV width, respectively. The blue dotted line shows the sum of the experimental *Monomer* and modeled *Surface* and *Bulk* contributions.

The *Total* spectrum peaks at a higher kinetic energy than the monomer spectrum, due to the contributions from clusters. The shift of the modeled contributions is applied according to the Born model; while the photoionization process changes the charge of the atom from 0 to $+e$, the *KLL* Auger decay marks a transition from $+e$ to $+2e$ [see Eqs. (4) and (5)]. According to Born's law [Eq. (2) with $z = 1$], the energetic shift of the Auger transition is $\Delta E^{\mathrm{Auger}}_{1\rightarrow 2} = (2 \times 1 + 1) \times \Delta E_1 = 3 \times \Delta E_1$. Consequently, the kinetic energy shifts for the *KLL* Auger electrons were set to 1.98 and 2.85 eV for surface and bulk atoms, respectively. Both cluster contributions have been convolved with Gaussians, thereby accounting for cluster-specific broadening effects that arise mainly due to the cluster size distribution. Moreover, the contributions of the monomer and the modeled surface and bulk spectra were scaled by the respective intensity ratios, which were determined from the $2p$ photoelectron spectrum. The experimental spectrum is well represented by the sum of the experimental monomer and the modeled cluster contributions, which becomes evident when optimizing the Gaussian widths used for the convolution. The best agreement to the experimental spectrum was found by optimizing the modeled Gaussian widths using the differential evolution algorithm as implemented in SciPy [49], which is based on the original method by Storn and Price [50], yielding widths of 0.85 eV for both the surface and bulk components. Here and in the following, the standard deviation of the Gaussian is referred to as the Gaussian width. The differential evolution method, which is also applied for optimizations in the following sections, is a stochastic approach to find the minimum of a multivariate function. As it is not gradient based, it is useful for finding global minima of the used difference function. It does not, however, return any uncertainty on the fit parameters [49,50]. The agreement of the experimental data with the predictions of the Born model lets us conclude that the Born model is a good approximation to describe the difference in solvation energy between a singly charged and a doubly charged ion in the same homogeneous environment.

Note that measuring the 1*s* photoelectron spectrum and the *KLL* Auger spectrum intrinsically yields the binding energy of the $Ar^{2+}(2p^{-2})\ ^1D_2$ double core-hole (DCH) state. The formation of such DCH states through decay from deeper holes or one-photon-two-electrons processes has been described for isolated atoms and molecules [34,51,52]. Recent investigations demonstrate a great potential of DCH spectroscopy using sequential multiphoton absorption at x-ray free-electron lasers [53,54]. To the best of our knowledge, however, DCH states in weakly bound matter have only been identified by their Auger decay [55], but no DCH binding energies in a medium have been reported so far. Our measurements align with the literature value for the atomic $Ar^{2+}(2p^{-2})\ ^1D_2$ state of 545.8 eV [35] and the observed shift results in values of 543.2 ± 0.2 eV for the surface and 542.0 ± 0.2 eV for the bulk of Ar clusters.

Figure 4 shows the high-resolution electron spectrum of Ar in the kinetic energy range between 180 and 234 eV, excited by a photon energy of 3300 eV, i.e., above the Ar 1*s* ionization threshold. The monomer spectrum (solid black line) shows the well-known Auger transitions, consisting of several contributions connected with the decay of Ar *L*-shell vacancies. Using the experimental results from Refs. [33, 35], these features are assigned to specific transitions. To the right of the vertical dashed line at 210 eV, only the *LMM*(1) Auger transitions $Ar^{2+}(2p^{-2}) \rightarrow Ar^{3+}(2p^{-1}3p^{-2})$ [33,35] have significant contributions. In Fig. 4, the assignments in the energy range of 180–210 eV show overlapping Auger transitions of different charge states and, therefore, of different energy shifts. Because of this, the following analysis focuses on the energy range 210–235 eV. The *Total* spectrum, which contains contributions from monomers and clusters alike, exhibits no clearly distinguishable features in that energy range but a pronounced shift of intensities to higher kinetic energies. As described above for

the $KL_{2,3}L_{2,3}$ decay, modeled cluster contributions are displayed in Fig. 4 as well. Their energy shift is chosen according to Eq. (2), with charge state $z = 2$. Consequently, the kinetic energy shifts for the *LMM*(1) Auger electrons were set to be $\Delta E_{2\to3}^{\text{Auger}} = (2 \times 2 + 1) \times \Delta E_1 = 5 \times \Delta E_1$, resulting in 3.30 and 4.75 eV for surface and bulk atoms, respectively. The cluster features are convoluted with Gaussians to account for broadening and then scaled to each other according to the respective intensity ratios determined from the 1*s* photoelectron spectrum. The modeled spectrum is in excellent agreement with the experimental spectrum, which is again demonstrated by optimizing the Gaussian widths that are used for the convolution. By using a differential evolution algorithm [49,50], widths of 2.0 and 1.5 eV were found for the surface and bulk components, respectively. Therefore, we conclude that the Born model is a good approximation to describe the solvation energy for ions with up to three elementary charges in a homogeneous cluster.

B. Ar clusters—coincidence spectra

The high-resolution approach presented in the previous section is only applicable up to the *LMM*(1) Auger step $[Ar^{2+}(2p^{-2}) \to Ar^{3+}(2p^{-1}3p^{-2})]$ in Ar clusters, since the following *LMM*(2) step $[Ar^{3+}(2p^{-1}3p^{-2}) \to Ar^{4+}(3p^{-4})]$ lies in a spectral region where the charge states of the levels involved in the Auger transitions cannot be disentangled without coincidence spectroscopy [33,35] (see above). For the experimental investigation of an Auger transition from charge state +3 to +4, it is therefore necessary to apply coincident electron detection.

Along the pathway in Eqs. (4)–(7), a total of four electrons are emitted from Ar. Therefore, data sets with exactly four electrons detected in coincidence following one excitation pulse have been analyzed. The coincident detection allows for applying filter conditions to the data, i.e., reducing the dataset to those events for which one or more of the detected electrons occur in a specific window of kinetic energies. This way, a specific decay cascade [like that in Eqs. (4)–(7)] can be separated from other channels.

For an exciting photon energy of 3600 eV, fourfold coincidence events have been filtered for the kinetic energy of the second electron (e_2^-) to be about 394 eV, identifying this as the Ar 1*s* photoelectron [47]. The acceptable kinetic energy range of the first electron (e_1^-) has then been set by a second filter to be between 2612 and 2680 eV, which is the range for the $KL_{2,3}L_{2,3}$ Auger electron [56,57], restricting the coincidence events to processes involving the $2p^{-2}$ intermediate state. When filtering on the $KL_{2,3}L_{2,3}$ Auger electron, the energy limits were deliberately set to cover a large range, as the experimental resolution in the required energy range does not allow a distinction between the individual fine-structure peaks of the $KL_{2,3}L_{2,3}$ spectrum.

The energy distribution of the remaining two electrons provides the structure of the *LMM*(1) (e_3^-) and *LMM*(2) (e_4^-) Auger electrons that are of interest. In order to extract the contribution of clusters to the total measured spectrum, the atomic contribution is subtracted using the data from a monomer reference measurement after intensity normalization in the range

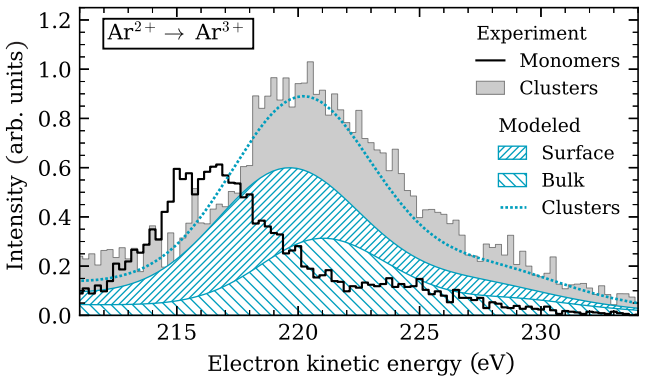

FIG. 5. Coincident Ar *LMM*(1) Auger spectra $[Ar^{2+}(2p^{-2}) \to Ar^{3+}(2p^{-1}3p^{-2})]$ measured from Ar monomers (black, solid line) and from Ar clusters (gray, filled area), the latter obtained by subtraction of the atomic reference spectrum from the mixed cluster/monomer jet. Additionally, modeled cluster contributions, consisting of surface and bulk contributions, are depicted (blue, hatched areas). The blue dotted line represents the sum of the modeled surface and bulk signals. Note the similarity to the high-energy part of Fig. 4.

$E_{\text{kin}}(e_3^-)$ between 215 and 217 eV and $E_{\text{kin}}(e_4^-)$ between 184 and 186 eV. This energy window is chosen because, as seen in the recorded spectra, there are only minor contributions from clusters.

In Figs. 5 and 6, the monomer and cluster spectra of the *LMM*(1) and *LMM*(2) Auger processes described by Eqs. (6) and (7) are shown, respectively. Comparing the experimental monomer and cluster spectra in Figs. 5 and 6, a significant energy shift is observed. In order to quantify this shift, modeled cluster contributions are displayed analogously to the analysis of the spectra in Figs. 3 and

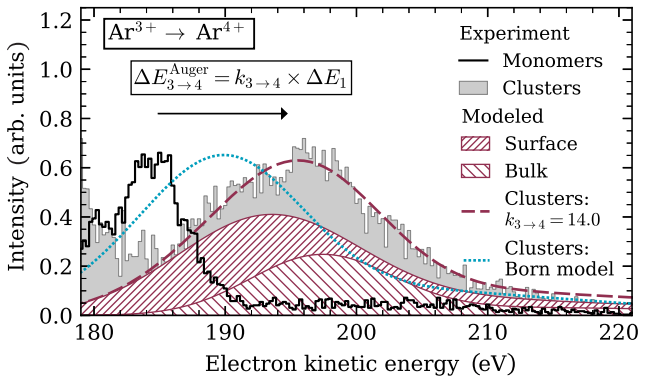

FIG. 6. Coincident Ar *LMM*(2) Auger spectra $[Ar^{3+}(2p^{-1}3p^{-2}) \to Ar^{4+}(3p^{-4})]$ measured from Ar monomers (black, solid line) and from Ar clusters (gray, filled area), the latter obtained by subtraction of the atomic reference spectrum from the cluster measurement. Additionally, modeled cluster contributions, obtained by shifting, broadening, and scaling the monomer spectrum, are displayed. The blue dotted line shows the modeled cluster spectrum according to the Born model, while a larger shift factor $k_{3\to4} = 14.0$ is used to model the red dashed curve, which fits the experimental spectrum. The surface and bulk components of the modeled spectrum are displayed as well (red, hatched areas).

4 and compared to the experimental data. Those modeled contributions consist of two instances of the monomer spectrum that are shifted in energy and broadened by convolution with a Gaussian, once for cluster surface and once for cluster bulk.

For this approach, boundary conditions, like the intensity ratio between surface and bulk contributions as well as their individual kinetic energy shifts, were applied. First, the ratio of the surface and bulk contributions was kept at 2.1, like in Fig. 4. As experiments I and II were conducted with the same cluster source using similar cluster-jet parameters, we assume for both experiments a similar cluster size distribution. As the cluster-to-monomer intensity ratio could not be determined for the coincidence experiment, the intensities of the monomer and cluster spectra are scaled manually to each other for better comparability. Then, the energy shift has been determined according to Eq. (2) using the single core-hole binding energy shift ΔE_1 determined in experiment I (see Appendix B). For the *LMM*(1) spectrum (Fig. 5), the cluster contribution is displayed using $2z + 1 = 5$ as predicted by the Born model [Eq. (2)]. The surface and bulk components were convolved with Gaussians of 2.0 and 1.5 eV width, respectively (see Sec. III A for further information). The *LMM*(1) spectrum can be compared to the high-resolution spectrum seen in Fig. 4. Both spectra are consistent, and the agreement with the predictions of the Born model is confirmed.

Similarly, modeled curves are shown for the *LMM*(2) spectrum in Fig. 6, but for two different energy shifts. The spectrum labeled *Clusters: Born model* uses the factor $2z + 1 = 7$, as predicted by Eq. (2). Here, a significant discrepancy between the prediction and the experiment is observed. A better agreement with the measured spectrum is achieved by employing a different shift factor $k_{3\to4}$, which is obtained by minimizing the difference between the modeled and the experimental curve using a differential evolution algorithm [49,50]. In addition, optimized values for the Gaussian widths $W_{3\to4}$ were obtained using this method. As discussed in Sec. III A, the applied fitting method is not gradient based, making it useful for finding global minima of the difference function. This is advantageous because the different combinations of widths, shifts, and amplitudes allow multiple local minima. The disadvantage is that no uncertainties on the fit parameters are returned.

In order to determine an uncertainty of the fit result that represents the uncertainty of the most impacting fixed parameters, i.e., the surface-to-bulk intensity ratio $I_{S/B}$ and the binding energy shift ΔE_1, Monte Carlo error propagation is used, sampling these parameters according to their estimated variance and covariance. As ΔE_1 is a fixed parameter in the fit of the Ar 1*s* photoelectron spectrum, it is sampled from a truncated Gaussian distribution that reflects its uncertainty. A standard deviation of 0.02 eV and an upper bound at $\Delta E_{1,S,\,max} = 0.664$ eV are chosen for the latter distribution to compare with experimental results from literature [4,58,59]. The differential evolution fit is performed for 10 000 samples. The central value of each derived quantity ($k_{3\to4}$, $W_{S,3\to4}$, and $W_{B,3\to4}$) was taken as the median of its Monte Carlo distribution, with uncertainties defined by the 2.5th and 97.5th percentiles. The results are $k_{3\to4} = 14.0^{+0.8}_{-0.6}$, $W_{S,3\to4} = 6.34^{+0.20}_{-0.16}$ eV, and $W_{B,3\to4} = 4.56^{+0.15}_{-0.12}$ eV. The discrepancy to the prediction of the Born model is further discussed in Sec. III D.

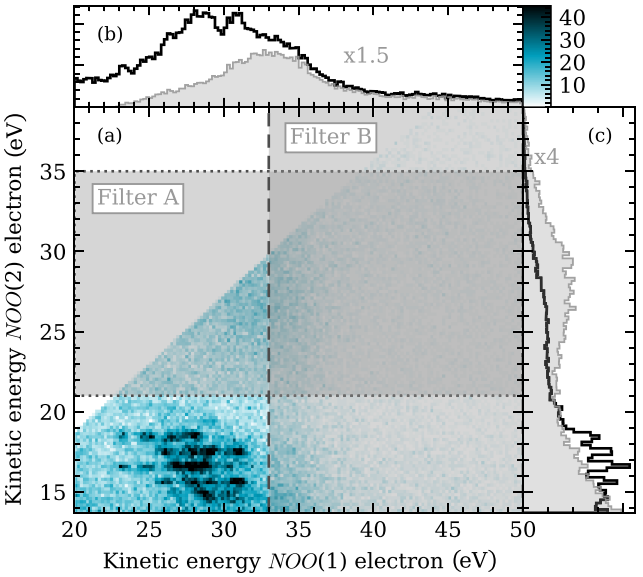

FIG. 7. (a) Electron-electron coincidence map of the *NOO*(1) and *NOO*(2) Auger electrons (e_2^- vs e_3^-) measured from a partially condensed Xe cluster jet. The ranges of Filter A and B [see text and Eqs. (14) and (15)] are depicted as gray patches in the coincidence map. (b) Black solid line: Intensity integrated along the kinetic energy of the *NOO*(2) electron as a function of the *NOO*(1) kinetic energy. Gray solid line: Integrated intensity of the filter range A, magnified by a factor of 1.5. (c) Black solid line: Intensity integrated along the kinetic energy of the *NOO*(1) electron as a function of the *NOO*(2) kinetic energy. Gray solid line: Integrated intensity of the filter range B, magnified by a factor of 4.

C. Xe clusters—coincidence spectra

For investigating whether the observed deviation from the Born model is only characteristic for Ar clusters or whether a more general conclusion can be drawn for other rare-gas clusters, we have also investigated Xe clusters ($\langle N \rangle = 30$). The transitions of interest are the two *NOO* Auger decays from the $4d^{-2}$ double core-hole state in Xe according to Eqs. (10) and (11). The $4d^{-2}$ state is efficiently populated through $3d$ photoionization and a subsequent *MNN* Auger decay [31]. For an exciting photon energy of 688 eV fourfold coincidence events have been filtered for the kinetic energy of the fourth electron (e_4^-) to be about 11.6 eV [47], identifying this as the Xe $3d_{5/2}$ photoelectron. The acceptable kinetic energy range of the first electron (e_1^-) has been set to be between 510 and 540 eV [31,60], which is the range of the $M_5N_{4,5}N_{4,5}$ Auger electron, restricting the coincidence events to processes involving the $4d^{-2}$ intermediate state. A distinction of electrons from monomers and clusters in the $M_5N_{4,5}N_{4,5}$ Auger spectra is beyond the present experimental resolution. The energy distribution of the remaining two electrons represents the structure of the *NOO*(1) (e_2^-) and *NOO*(2) (e_3^-) Auger decays. The energy correlation between e_2^- and e_3^- is displayed in Fig. 7 in a coincidence map.

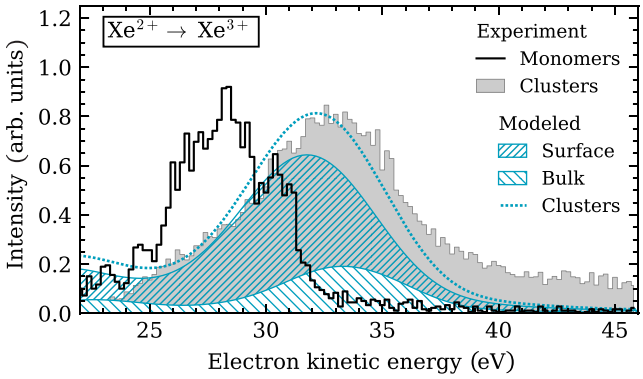

FIG. 8. Coincident Xe *NOO*(1) Auger spectra [$Xe^{2+}(4d^{-2}) \rightarrow Xe^{3+}(4d^{-1}5p^{-2})$] measured from Xe monomers (black, solid line) and from Xe clusters (gray, filled area). The cluster spectrum is extracted by applying Filter A [see Eq. (14)]. Additionally, modeled cluster contributions for surface and bulk are depicted (blue, hatched areas). The blue dotted line represents the sum of the modeled surface and bulk signals.

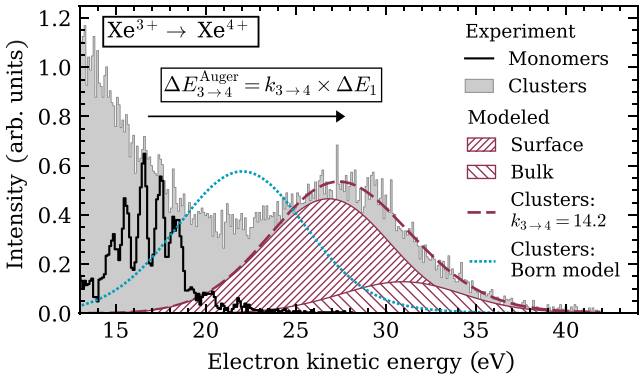

FIG. 9. Coincident Xe *NOO*(2) Auger spectra [$Xe^{3+}(4d^{-1}5p^{-2}) \rightarrow Xe^{4+}(5p^{-4})$] measured from Xe monomers (black, solid line) and from Xe clusters (gray, filled area). The cluster spectrum is extracted by applying Filter B [see Eq. (15)]. The low-energy contribution to the cluster spectrum is associated with a different *NOO*(2) Auger channel, namely, the decay $Xe^{3+}(4d^{-1}5p^{-2}) \rightarrow Xe^{4+}(5s^{-1}5p^{-3})$ (see Fig. 2), which is not further analyzed here. In addition to the experimental spectra, modeled cluster contributions, obtained by shifting, broadening, and scaling the monomer spectrum, are displayed. The blue dotted line shows the modeled cluster spectrum according to the Born model, while a different shift factor $k_{3\rightarrow4} = 14.2$ is used to model the red dashed curve, which fits the experimental spectrum. The surface and bulk components of the modeled spectrum are displayed as well (red, hatched areas).

The further data analysis is similar to the approach described in Sec. III B. However, since in specific cases the subtraction of the atomic contributions is less straightforward than for argon, we use a different approach to obtain the cluster contributions. In detail, for Xe, it is possible to filter the measured multielectron coincidence events in a way that monomer contributions are excluded by setting appropriate conditions to at least one of the detected electrons. Such conditions were obtained by comparison with the energy ranges of the emitted electrons in reference measurements of the monomers [34]:

$$22.7\,\text{eV} < E_{\text{kin}}(e^-_{NOO(1),\text{atomic}}) < 31.5\,\text{eV}, \tag{12}$$

$$13.0\,\text{eV} < E_{\text{kin}}(e^-_{NOO(2),\text{atomic}}) < 19.0\,\text{eV}. \tag{13}$$

Since the kinetic energies of Auger electrons from the clusters are shifted to higher values, we can define conditions that *exclude* any atomic contribution. The spectrum of the *NOO*(1) Auger electron in clusters is obtained by applying the condition

$$\underline{\text{Filter A:}} \quad 21\,\text{eV} < E_{\text{kin}}(e_3^-) < 35\,\text{eV} \tag{14}$$

to the *NOO*(2) Auger electron (e_3^-), which is above its energy range for monomers. In turn, a pure cluster spectrum of the *NOO*(2) Auger electron is obtained accordingly by applying the condition

$$\underline{\text{Filter B:}} \quad 33\,\text{eV} < E_{\text{kin}}(e_2^-) < 50\,\text{eV} \tag{15}$$

to the *NOO*(1) Auger electron (e_2^-). Because spectra from Xe monomers cannot fulfill these conditions, other electrons that are measured in coincidence with Filter A or B must have been emitted from clusters. The impact of applying filters is demonstrated in Fig. 7. It should be noted that while all monomer contributions are removed from the spectra using these conditions, part of the cluster signal is omitted as well. The exact shape and energy distribution of the resulting cluster spectrum may therefore be distorted.

In Figs. 8 and 9, the spectra of the $N_{4,5}O_{2,3}O_{2,3}(1)$ and $N_{4,5}O_{2,3}O_{2,3}(2)$ Auger electrons are shown. In both figures, the solid black curves show the spectra of a pure monomer target. The gray-filled curve was obtained from a partially condensed cluster jet (containing both atoms and clusters) but using Eq. (14) or (15), respectively, to exclude the monomer contributions. Both spectra are scaled arbitrarily for better comparability. Similar to the results for Ar clusters (see Sec. III B), a clear difference between the predicted energy shift by the Born model and the present measurement for an Auger transition starting from a charge state of +3 is observed. Quantitatively, the energy shifts and the intensity ratio of surface and bulk contributions have been derived from the Xe cluster 4*d* photoelectron spectrum recorded at 110 eV exciting photon energy. They were determined to be $\Delta E_{1,\text{S}} = 730 \pm 17$ meV for surface and $\Delta E_{1,\text{B}} = 1020 \pm 17$ meV for bulk, with an intensity ratio of $I_{\text{S/B}} = 3.7$ (see Appendix B for further details).

For the *NOO*(1) spectrum, the cluster contribution has been modeled using an energy shift of $\Delta E^{\text{Auger}}_{2\rightarrow3} = 5 \times E_1$ according to Eq. (2). Convoluting the modeled spectra with Gaussians of width 2.0 and 1.5 eV achieves a reasonable agreement with the experimental spectrum, although the peak position of the experimental spectrum is not exactly reproduced by the modeled curve. This is most likely caused by the spectral distortion that occurs due to nearly equally fast electrons in coincident particle detection that is described in Sec. II, and that is graphically demonstrated by the cutoff close to the diagonal in Fig. 7, where $E_{\text{kin}}(e^-_{NOO(2)}) \simeq E_{\text{kin}}(e^-_{NOO(1)})$. Here, this distortion changes the relative intensities in the measured

cluster *NOO*(1) spectrum and, therefore, shifts its central energy to a higher value compared to the actually emitted spectrum.

For the *NOO*(2) spectrum in Fig. 9, the shift predicted by the Born model ($\Delta E_{3\to4}^{\text{Auger}} = 7 \times \Delta E_1$) does not properly reproduce the experimental spectrum, which agrees with the findings from the Ar *LMM*(2) case. The same method as in Sec. III B is used to determine the optimal parameters for the energy shift and the spectral widths.

Specifically, the two modeled contributions, representing the surface and bulk contributions to the cluster spectrum, are fitted to the experimental cluster spectrum, whereas each modeled contribution is defined as an energy-shifted and artificially broadened instance of the experimental monomer spectrum. The fit parameters for the applied differential evolution algorithm (for further information, see Secs. III A and III B) are the Gaussian widths $W_{3\to4}$ used for the broadening, a factor $k_{3\to4}$ that determines the energy shift with respect to ΔE_1, and a scaling factor to match the intensities of the spectra. The energy shift ΔE_1 and the intensity ratio of the surface and bulk components $I_{\text{S/B}}$ are fixed during the fitting procedure. As discussed previously, no uncertainties on the fit results are obtained from the differential evolution algorithm. In order to still accommodate the uncertainties of the fixed parameters ΔE_1 and $I_{\text{S/B}}$, Monte Carlo error propagation is used, sampling both parameters according to their estimated covariance. By fitting the experimental spectrum for each sampled Monte Carlo realization ($N = 10\,000$), a distribution of results is obtained whose uncertainty represents the uncertainty of the input parameters.

For each of the derived quantities, the central value was taken as the median of its Monte Carlo distribution, with the uncertainties defined by the 2.5th and 97.5th percentiles. In the case of $k_{3\to4}$, this uncertainty is combined in quadrature with the systematic uncertainty $2\sigma_{\Delta E_1} = 34\,\text{meV}$ that is induced by the conversion function (see Appendix B). The results are $k_{3\to4} = 14.2^{+1.4}_{-2.0}$, $W_{\text{S},3\to4} = 2.76^{+0.50}_{-0.17}\,\text{eV}$, and $W_{\text{B},3\to4} = (2.65 \pm 0.22)\,\text{eV}$. The discrepancy of this result with the predictions of the Born model is further discussed in Sec. III D.

D. Discussion

The analysis of the experimental data shows that the predictions of the Born model for Auger electron energies are reasonable for decays to charge states up to +3 in rare-gas clusters. For transitions to quadruply charged states, significant deviations from the model are observed. In this case, the experimentally observed shift is considerably larger than predicted by the Born model, namely, $14.0^{+0.8}_{-0.6} \times \Delta E_1$ for Ar and $14.2^{+1.4}_{-2.0} \times \Delta E_1$ for Xe, instead of $7 \times \Delta E_1$.

Assigning overall quantitative uncertainties for the determined values of $k_{3\to4}$ is challenging. By applying Monte Carlo error propagation, a statistical uncertainty of the fit results is obtained, depending on the variance of the most impacting and uncertain parameters, i.e., the solvation energy of the singly charged ion ΔE_1 and the intensity ratio of surface and bulk signals $I_{\text{S/B}}$. However, it is hardly possible to quantify the systematic influence of the coincidence filtering procedure on the exact shape of the experimental spectra. A qualitative distortion due to the coincidence conditions is assessed to be irrelevant for the Ar spectra (shown in Figs. 5 and 6) but likely for the Xe spectra presented in Figs. 7– 9. However, the evaluation of the Xe data using different coincidence filters did not result in qualitatively different outcomes. In the following, possible explanations for the observed behavior are discussed.

In extended systems like clusters, nonlocal relaxation mechanisms, which compete with the local decay [7], can contribute to the electron signal at higher kinetic energies. Most prominently, core-level interatomic Coulombic decay (cICD) is known to compete with the Auger decay, albeit with a small branching ratio [28,61]. For the +3 to +4 transition, however, the kinetic energies of the cICD electrons are expected to be even higher than the observed shifts in our experiments. Consequently, the cICD process is expected not to contribute to the measured signal.

Regarding the validity of the Born model, it should be noted that this is a simplified model considering the electrostatic energy of an ion, idealized as a charged sphere with well-defined radius r_i, which is embedded in a continuous, isotropic, and polarizable medium. This approximation does not account for all effects relevant to the present spectra. For example, orbital-dependent core-level binding energy shifts ΔE_1 have been reported [26], which is in contrast to the assumption of identical ΔE_1 for all core shells used in the present work. Furthermore, delocalization of outer valence orbitals and overlap with the neighbor's valence orbitals may result in a bandlike electronic structure [8]. The latter effect leads to a much broader energy distribution and a significantly lower first ionization potential for these orbitals [4,8]. Additionally, valence holes created during multistep Auger cascades in solids were observed to dynamically change energy inside the valence band during subsequent Auger decays, increasing their energetic width [62]. Therefore, it is reasonable to expect deviations of measurements from the Born model, if the Auger decay produces an increasing number of holes in valence orbitals. If, however, the involvement of valence orbitals in a transition were the decisive factor for the shift, deviations should be observable for the *LMM*(1) and *NOO*(1) transitions as well. Instead, it is conceivable that the presence of already existing valence holes, created at an earlier stage, influences the potentials in the vicinity of the ion and, therefore, the effect of polarization. For instance, contractions of the cationic radii, as a consequence of the increasing effective nuclear charge, may occur. If the spatial extension of the cations is indeed reduced during the relaxation pathways, larger energy differences to the monomer are expected than for a fixed ionic radius [see Eq. (A6)]. Furthermore, changes of the cluster structure, i.e., contraction of shells or reorganization of the cluster lattice around the ion would impact the effective cationic radius and the local permittivity of the medium. If we assume that the sudden deviation from the Born model in the $z = +3$ to +4 step is an effect that purely originates from dynamical behavior in the cluster, which is associated with structural changes that influence the effective ion radius or the polarizability of the medium, a saturation of this effect can be expected. This may be, e.g., due to the limited contraction of the ion and the first solvation shell or due to the saturation of the polarization in the surrounding

atoms. For an unambiguous statement, we encourage further experiments on different systems and theoretical modeling.

IV. CONCLUSIONS

Auger cascades are the dominant decay pathways for inner-shell ionization events occurring in a wide photon-energy range from the soft to hard x-ray regime, leading to multiply charged ions. In this study, we experimentally quantified a gradually increasing kinetic energy shift of Auger electrons emitted from intermediate-sized rare-gas clusters in comparison to the monomer transitions along a multistep Auger cascade. Although the magnitude of this shift, which originates from an electron binding energy shift caused by polarization screening, is reasonably described by the Born model for the first three (auto)ionization events, it deviates considerably for the transition from $+3$ to $+4$. Note that the observed behavior is not yet described by other existing implicit solvent models, which may, therefore, benefit from further insights about the ion charge dependence of solvation energies as well. Aspects potentially explaining this deviation have been discussed, such as the limits of the model, the shell-dependent core-level binding energy shifts, the delocalization of valence orbitals, and structural changes in the cluster lattice. From the present data, their individual influence and how this deviation will develop for higher charge states remain unclear. Further experimental work and theoretical modeling are thus warranted. For example, investigations of Auger decays to highly charged states, where all of the involved orbitals are localized core orbitals, could provide further information. Such experiments are, however, challenging. Nevertheless, our results contribute to the interpretation of complex electron spectra of extended systems exposed to high-energy radiation and serve as a starting point for further research on the energetics of ions embedded in an environment.

ACKNOWLEDGMENTS

The authors acknowledge MAX IV Laboratory for time on the beamline FinEstBeAMS under Proposal No. 20220215. Research conducted at MAX IV, a Swedish national user facility, is supported by the Swedish Research Council (VR) under Contract No. 2018-07152, the Swedish Governmental Agency for Innovation Systems Vinnova under Contract No. 2018-04969, and Formas under Contract No. 2019-02496. We acknowledge Jenni Autio and Teemu Salmela for their assistance during the FinEstBeAMS experimental campaign. We acknowledge SOLEIL for provision of synchrotron radiation facilities (beamline GALAXIES under Proposals No. 20210253 and No. 20231099). We acknowledge Dominique Prieur and Jean-Pascal Rueff for their support. This work was supported by the German Federal Ministry of Education and Research (BMBF) through Projects No. 05K22RK2—GPhaseCC and No. 05K22RK1—TRANSALP and by the Deutsche Forschungsgemeinschaft (DFG, German Research Foundation)—Project No. 328961117—SFB 1319 ELCH (extreme light for sensing and driving molecular chirality). M.P. acknowledges the Research Council of Finland for financial support (including The University of Oulu and Research Council of Finland Profi5—Project No. 326291). E.P. acknowledges support from the Research Council of Finland and the Finnish Cultural Foundation (North Ostrobothnia Regional Fund). O.B. acknowledges support from the Swedish Research Council VR through Project No. 2023-04346.

DATA AVAILABILITY

The data that support the findings of this article are not publicly available upon publication because it is not technically feasible and/or the cost of preparing, depositing, and hosting the data would be prohibitive within the terms of this research project. The data are available from the authors upon reasonable request.

APPENDIX A: THE BORN MODEL

In the Born model, the electrostatic contribution to the solvation energy of an ion is determined by assuming the ion to be a charged sphere of charge ze and radius r_i that is embedded in a continuous, isotropic, and polarizable dielectric medium. In this scenario, the electrostatic energy U of the introduced charge is given by integrating the energy density of the electric field over the volume V outside of the charged sphere [9]:

$$U_{\text{medium}} = \frac{\varepsilon_0 \varepsilon_r}{2} \int |\vec{E}| \mathrm{d}V, \tag{A1}$$

where ε_0 and ε_r are the permittivity of free space and the relative permittivity of the medium, respectively. Using the absolute value of the electric field strength $|\vec{E}| = (ze)/(4\pi\varepsilon_0\varepsilon_r r^2)$, a simple expression is obtained:

$$U_{\text{medium}} = \frac{\varepsilon_0 \varepsilon_r}{2} \int_{r_i}^{\infty} \left(\frac{ze}{4\pi\varepsilon_0\varepsilon_r r^2} \right)^2 4\pi r^2 \mathrm{d}r \tag{A2}$$

$$= \frac{z^2 e^2}{8\pi\varepsilon_0\varepsilon_r} \int_{r_i}^{\infty} \frac{1}{r^2} \mathrm{d}r \tag{A3}$$

$$= \frac{z^2 e^2}{8\pi\varepsilon_0\varepsilon_r r_i}. \tag{A4}$$

When calculating the difference between this energy and the energy U_0, when the ion is not surrounded by any medium, a quadratic dependence on the ion's charge z is found:

$$\Delta E_z = U_{\text{medium}} - U_0 \tag{A5}$$

$$= -\frac{z^2 e^2}{8\pi\varepsilon_0 r_i} \left(1 - \frac{1}{\varepsilon_r} \right). \tag{A6}$$

In this model, the electrostatic energy difference between an isolated ion and an embedded ion, which are in the same electronic state, solely depends on the charge of the ion z, its radius r_i, and the permittivity ε_r of the medium. Assigning a radius to an ion is, however, only an approximation in the framework of this model, as there is no unified definition of an ionic radius.

APPENDIX B: FIT ANALYSIS OF THE PHOTOELECTRON SPECTRA

For a comparison of the experimental Auger electron spectrum with the predictions of the Born model, the solvation energy of the singly charged ion must be determined using photoelectron spectroscopy. In this Appendix, a brief overview about the energetics in photoelectron spectroscopy of clusters is given and the fitting procedure is described.

The solvation energy ΔE_z in clusters is not constant but depends, in our case, on the elemental composition (Ar or Xe), on the size of the clusters, and on the site of the respective atom. The elemental specificity is clearly given by the influence of the ionic radius r_i and the permittivity of the environment ε_r, i.e., its element-specific polarizability. Hence, different values for ΔE_z are expected for Ar and Xe clusters. Furthermore, the polarization of its environment by a single ion and, therefore, the magnitude of polarization screening also depend on the position of the ion in the cluster [6], i.e., how many polarizable atoms surround the ion. Depending on the number of nearest neighbors of the respective site of an atom, sites can be categorized into bulk and surface, where bulk atoms experience a larger polarization screening [5,59]. Surface sites can be further divided into corner, edge, and face with an increasing number of nearest neighbors. This division has been observed by high-resolution electron spectroscopy [5]. It leads to a broader distribution of solvation energies among surface atoms. The cluster size itself is decisive for the relative abundance of sites [5,42] but also impacts the value of solvation energy for each site, i.e., larger cluster sizes lead to larger solvation energies. Additionally, the cluster size distribution in the present experiments is broad. The final photoelectron spectrum will reflect these distributions of different cluster sites and sizes. The measured photoelectron spectra, in turn, are also significantly influenced by the kinetic-energy-dependent attenuation length of electrons in clusters [48]. Therefore, we expect similar surface-to-bulk and cluster-to-atom ratios in the photoelectron and Auger spectra if the kinetic energies of the electrons are in the same range.

In order to determine the binding energy difference of Ar surface and bulk components with respect to Ar monomers, a least-squares fit is performed on the Ar $2p$ photoelectron spectrum, measured at an exciting photon energy of $h\nu = 2920\,\mathrm{eV}$ using a high-resolution hemispherical electron analyzer. This spectrum is displayed in Fig. 10(a). Six Voigt profiles on top of a constant background are used to fit the experimental curve. The Voigt model, which is implemented in the used LMFIT Python package [63], allows a description of the measured spectral line shape that is governed by the Gaussian shape of the spectrometer resolution and the Lorentzian shape of the lifetime broadening, which is about 112 meV [64]. The Voigt model is defined as

$$V(x;A,\mu,\sigma,\gamma) = \frac{A\mathrm{Re}[w(z)]}{\sigma\sqrt{2\pi}}, \tag{B1}$$

where

$$z = \frac{x-\mu+iy}{\sigma\sqrt{2}}, \tag{B2}$$

$$w(z) = e^{-z^2}\mathrm{erfc}(-iz), \tag{B3}$$

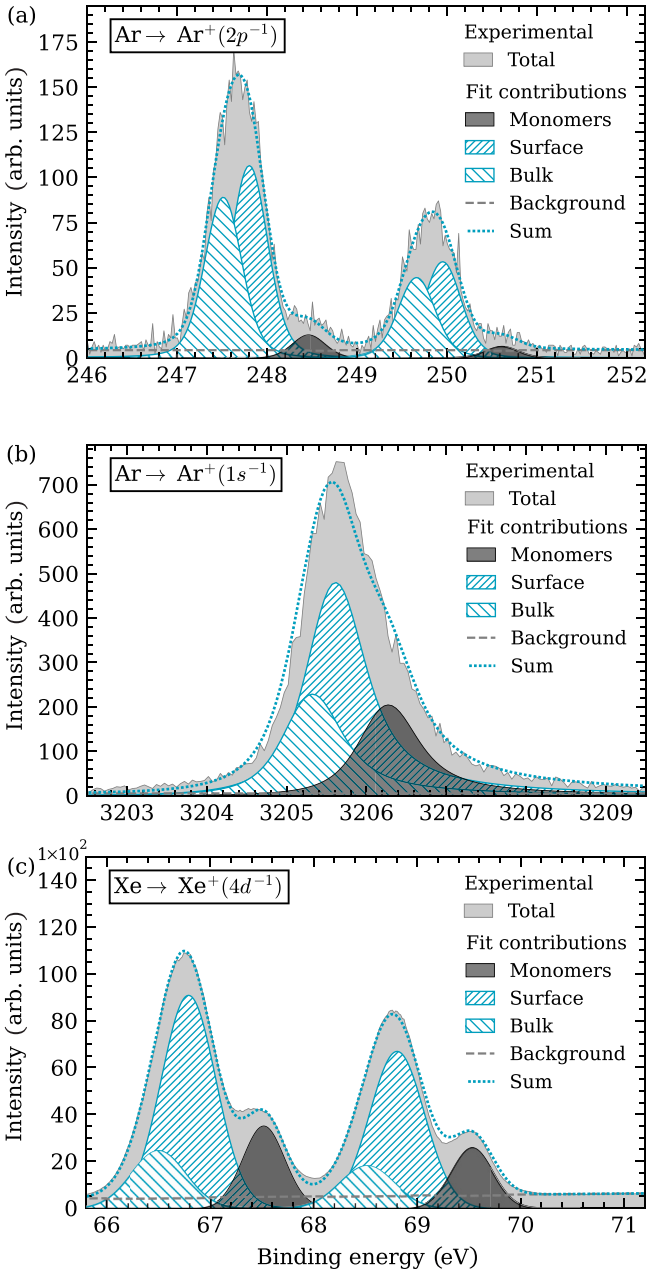

FIG. 10. Fitted photoelectron spectra of (a) Ar $2p$, (b) Ar $1s$, and (c) Xe $4d$. The experimental spectra (gray, filled area) contain a mixture of uncondensed monomers and clusters. The components of the fit represent the contribution of monomers (black, filled area), cluster surface atoms, and cluster bulk atoms (both blue, hatched areas) to the overall fitted spectrum (blue, dotted line).

and erfc() is the complementary error function. Due to the limited experimental resolution in all of the present photoelectron spectra, it is not possible to find an unambiguous solution for the decomposition of each photoelectron feature into three components (atom, surface, and bulk) without applying boundary conditions. Physical boundary conditions are applied to approach the most reasonable solution, i.e., the binding energy shift of surface features should not exceed

the values found in literature for large clusters [8,26,48,59], the binding energy difference between surface and bulk should not deviate significantly from the, rather constant, values reported in literature [8,26,48,59], and the width of the bulk features should not exceed the ones from surface features [8,26]. The latter constraint relates to the more diverse site distribution of surface atoms (corner, edge, and face) in comparison to bulk atoms. Additionally, the energies and intensities of spin-orbit components were forced to correspond to the spin-orbit characteristics of the respective atomic features. In the framework of these boundary conditions, a good estimate of the intensities and shifts of the cluster features is obtained.

The boundary conditions for the fit of the Ar $2p$ photoelectron spectrum specifically include that the binding energy shift of the surface contribution cannot exceed the values reported in literature for clusters of intermediate size ($\Delta E_{1,\mathrm{S}} \leqslant 0.66$ eV) [8] and that the binding energy shift of the bulk contribution with respect to the surface contribution is only within the small range of 0.27–0.31 eV as reported in Refs. [58,59]. The result of this fit is given in Table II. Most importantly, the binding energy differences $\Delta E_{1,\mathrm{S}}(2p^{-1}) = 0.66\,\mathrm{eV}$ and $\Delta E_{1,\mathrm{B}}(2p^{-1}) = 0.95\,\mathrm{eV}$ were determined for surface and bulk components, respectively. As the result for $\Delta E_{1,\mathrm{S}}$ is at the limits of the boundary conditions, no meaningful uncertainty for ΔE_1 is obtained from the fit. Considering the choice of boundary conditions and the consistency with results from literature [4,8], the obtained results are found to give the best representation of the cluster contributions to the photoelectron spectrum. Therefore, the determined intensity ratios are assumed to be representative of Ar electron spectra recorded at approximately 2.6 keV kinetic energy.

In order to determine the intensity ratio of surface and bulk components in the lower kinetic energy regime (180–235 eV), another photoelectron fit is performed using the Ar $1s$ photoelectron spectrum, which is shown in Fig. 10(b). This spectrum was recorded at an exciting photon energy of $h\nu = 3336\,\mathrm{eV}$, leading to a nominal kinetic energy of $\approx$130 eV. Here, three skewed Voigt profiles on a constant background are fitted to the experimental spectrum, in order to accommodate for the asymmetric line shape that is possibly caused by postcollision interaction [65]. The skewed Voigt profile is defined as

$$f(x;A,\mu,\sigma,\gamma,c) = V(x;A,\mu,\sigma,\gamma)\left\{1+\mathrm{erf}\left[\frac{c(x-\mu)}{\sigma\sqrt{2}}\right]\right\}, \tag{B4}$$

where erf() is the error function. For the fit, the binding energy differences obtained from the Ar $2p$ photoelectron fit are used as fixed input. The results, most prominently the intensity ratios $I_{\mathrm{S/B}} = 2.1$ and $I_{\mathrm{C/A}} = 3.5$, are given in Table II.

Finally, a fit of the Xe $4d$ photoelectron spectrum is performed to obtain information about the site distribution and energy shifts in Xe clusters in the present experiment. The fitted spectrum is displayed in Fig. 10(c). Six Gaussian profiles and a linear background are used to model the experimental curve. Here, Gaussian profiles are used instead of Voigt profiles because the width of the line shapes are majorly governed by the spectrometer resolution and not the lifetime broadening. The specific boundary conditions that are applied here include that the binding energy difference of the surface component is in the range known for Xe clusters of small to intermediate size ($0.6\,\mathrm{eV} \leqslant \Delta E_{1,\mathrm{S}} \leqslant 0.8\,\mathrm{eV}$ [59]), while the binding energy difference of the bulk component with respect to the surface component is fixed to 0.29 eV.

The fit yields binding energy differences $\Delta E_{1,\mathrm{S}}(4d^{-1}) = 0.73\,\mathrm{eV}$ and $\Delta E_{1,\mathrm{B}}(4d^{-1}) = 1.02\,\mathrm{eV}$ for surface and bulk components, respectively (see Table II). This is in good agreement with literature values for small Xe clusters ($\Delta E_{1,\mathrm{S,lit}} = 0.70\,\mathrm{eV}$ and $\Delta E_{1,\mathrm{B,lit}} = 1.01\,\mathrm{eV}$ for $\langle N\rangle \approx 90$ [59]) but is significantly lower than the values found for large Xe clusters ($\Delta E_{1,\mathrm{S,lit}} = 0.80\,\mathrm{eV}$ and $\Delta E_{1,\mathrm{B,lit}} = 1.11\,\mathrm{eV}$ for $\langle N\rangle \approx 300$ [59], $\Delta E_{1,\mathrm{S,lit}} = 0.83\,\mathrm{eV}$ and $\Delta E_{1,\mathrm{B,lit}} = 1.12\,\mathrm{eV}$ for $\langle N\rangle \approx 1000$ [8], and $\Delta E_{1,\mathrm{S,lit}} = 0.86\,\mathrm{eV}$ and $\Delta E_{1,\mathrm{B,lit}} = 1.15\,\mathrm{eV}$ for $\langle N\rangle \approx 1900$ [26]). The fit is, therefore, found to be a good representation of the spectral composition in the present experimental Xe spectra.

The results for the Xe photoelectron fit are dependent on the applied conversion function that transforms the raw time-of-flight data to kinetic energies. The conversion function has an uncertainty of $\delta E_{\mathrm{kin}} \approx 0.3\,\mathrm{eV}$ in the relevant range, which induces an uncertainty in the determined Xe $4d$ binding energy shift. Using the Jacobian and covariance matrix of the conversion function, a standard deviation of $\sigma_{\Delta E_1} = 17\,\mathrm{meV}$ is determined.

[1] M. N. Piancastelli, T. Marchenko, R. Guillemin, L. Journel, O. Travnikova, I. Ismail, and M. Simon, Hard x-ray spectroscopy and dynamics of isolated atoms and molecules: A review, Rep. Prog. Phys. **83**, 016401 (2020).

[2] V. L. Sukhorukov, I. D. Petrov, B. M. Lagutin, A. Ehresmann, K. H. Schartner, and H. Schmoranzer, Many-electron dynamics of atomic processes studied by photon-induced fluorescence spectroscopy, Phys. Rep. **786**, 1 (2019).

[3] E. Alizadeh, T. M. Orlando, and L. Sanche, Biomolecular damage induced by ionizing radiation: The direct and indirect effects of low-energy electrons on DNA, Annu. Rev. Phys. Chem. **66**, 379 (2015).

[4] O. Björneholm, F. Federmann, F. Fössing, T. Möller, and P. Stampfli, Core level binding energy shifts and polarization screening: A combined experimental and theoretical study of argon clusters, J. Chem. Phys. **104**, 1846 (1996).

[5] T. Hatsui, H. Setoyama, N. Kosugi, B. Wassermann, I. L. Bradeanu, and E. Rühl, Photoionization of small krypton clusters in the Kr *3d* regime: Evidence for site-specific photoemission, J. Chem. Phys. **123**, 154304 (2005).

[6] I. Mukatayev, G. D'Avino, B. Sklénard, V. Olevano, and J. Li, Electronic polarization effects in core-level spectroscopy, Phys. Rev. B **109**, L121109 (2024).

[7] T. Jahnke, U. Hergenhahn, B. Winter, R. Dörner, U. Frühling, P. V. Demekhin, K. Gokhberg, L. S. Cederbaum, A. Ehresmann, A. Knie, and A. Dreuw, Interatomic and intermolecular Coulombic decay, Chem. Rev. **120**, 11295 (2020).

[8] R. Feifel, M. Tchaplyguine, G. Öhrwall, M. Salonen, M. Lundwall, R. R. Marinho, M. Gisselbrecht, S. L. Sorensen, A. Naves De Brito, L. Karlsson, N. Mårtensson, S. Svensson, and O. Björneholm, From localised to delocalised electronic states in free Ar, Kr and Xe clusters, Eur. Phys. J. D **30**, 343 (2004).

[9] M. Born, Volumen und Hydratationswärme der Ionen, Z. Phys. **1**, 45 (1920).

[10] T. T. Duignan and X. S. Zhao, The Born model can accurately describe electrostatic ion solvation, Phys. Chem. Chem. Phys. **22**, 25126 (2020).

[11] B. Jayaram, R. Fine, K. Sharp, and B. Honig, Free energy calculations of ion hydration: An analysis of the Born model in terms of microscopic simulations, J. Phys. Chem. **93**, 4320 (1989).

[12] C. J. Stein, J. M. Herbert, and M. Head-Gordon, The Poisson-Boltzmann model for implicit solvation of electrolyte solutions: Quantum chemical implementation and assessment via Sechenov coefficients, J. Chem. Phys. **151**, 224111 (2019).

[13] A. V. Onufriev and D. A. Case, Generalized Born implicit solvent models for biomolecules, Annu. Rev. Biophys. **48**, 275 (2019).

[14] S. Miertuš, E. Scrocco, and J. Tomasi, Electrostatic interaction of a solute with a continuum. A direct utilizaion of *AB initio* molecular potentials for the prevision of solvent effects, Chem. Phys. **55**, 117 (1981).

[15] M. Cossi, V. Barone, R. Cammi, and J. Tomasi, *Ab initio* study of solvated molecules: A new implementation of the polarizable continuum model, Chem. Phys. Lett. **255**, 327 (1996).

[16] C. Azuara, E. Lindahl, P. Koehl, H. Orland, and M. Delarue, PDB_Hydro: Incorporating dipolar solvents with variable density in the Poisson-Boltzmann treatment of macromolecule electrostatics, Nucleic Acids Res. **34**, W38 (2006).

[17] C. Azuara, H. Orland, M. Bon, P. Koehl, and M. Delarue, Incorporating dipolar solvents with variable density in Poisson-Boltzmann electrostatics, Biophys. J. **95**, 5587 (2008).

[18] P. Koehl, H. Orland, and M. Delarue, Computing ion solvation free energies using the dipolar Poisson model, J. Phys. Chem. B **113**, 5694 (2009).

[19] S. Zhou, L. T. Cheng, J. Dzubiella, B. Li, and J. A. McCammon, Variational implicit solvation with Poisson-Boltzmann theory, J. Chem. Theory Comput. **10**, 1454 (2014).

[20] Y. Marcus, Thermodynamics of solvation of ions, J. Chem. Soc. Faraday Trans. **87**, 2995 (1991).

[21] R. W. Howell, Auger processes in the 21st century, Int. J. Radiat. Biol. **84**, 959 (2008).

[22] G. Moretti, Auger parameter and Wagner plot in the characterization of chemical states by X-ray photoelectron spectroscopy: A review, J. Electron Spectrosc. Relat. Phenom. **95**, 95 (1998).

[23] D. C. Haynes, *et al.*, Clocking Auger electrons, Nat. Phys. **17**, 512 (2021).

[24] D. Céolin, N. V. Kryzhevoi, C. Nicolas, W. Pokapanich, S. Choksakulporn, P. Songsiriritthigul, T. Saisopa, Y. Rattanachai, Y. Utsumi, J. Palaudoux, G. Öhrwall, and J. P. Rueff, Ultrafast charge transfer processes accompanying *KLL* Auger decay in aqueous KCl solution, Phys. Rev. Lett. **119**, 263003 (2017).

[25] F. Gel'mukhanov, M. Odelius, S. P. Polyutov, A. Föhlisch, and V. Kimberg, Dynamics of resonant x-ray and Auger scattering, Rev. Mod. Phys. **93**, 035001 (2021).

[26] M. Lundwall, R. F. Fink, M. Tchaplyguine, A. Lindblad, G. Öhrwall, H. Bergersen, S. Peredkov, T. Rander, S. Svensson, and O. Björneholm, Shell-dependent core-level chemical shifts observed in free xenon clusters, J. Phys. B: At. Mol. Opt. Phys. **39**, 5225 (2006).

[27] M. Lundwall, A. Lindblad, G. Öhrwall, S. Svensson, and O. Björneholm, Neighbor-induced photoelectron recapture in argon clusters: A photon-energy-dependent study of Auger spectra, Phys. Rev. A **78**, 065201 (2008).

[28] A. Hans, C. Küstner-Wetekam, P. Schmidt, C. Ozga, X. Holzapfel, H. Otto, C. Zindel, C. Richter, L. S. Cederbaum, A. Ehresmann, U. Hergenhahn, N. V. Kryzhevoi, and A. Knie, Core-level interatomic Coulombic decay in van der Waals clusters, Phys. Rev. Res. **2**, 012022(R) (2020).

[29] H. Fukuzawa, *et al.*, Deep inner-shell multiphoton ionization by intense x-ray free-electron laser pulses, Phys. Rev. Lett. **110**, 173005 (2013).

[30] A. Rörig, S.-K. Son, T. Mazza, P. Schmidt, T. M. Baumann, B. Erk, M. Ilchen, J. Laksman, V. Music, S. Pathak, D. E. Rivas, D. Rolles, S. Serkez, S. Usenko, R. Santra, M. Meyer, and R. Boll, Multiple-core-hole resonance spectroscopy with ultraintense X-ray pulses, Nat. Commun. **14**, 5738 (2023).

[31] Y. Tamenori, K. Okada, S. Nagaoka, T. Ibuki, S. Tanimoto, Y. Shimizu, A. Fujii, Y. Haga, H. Yoshida, H. Ohashi, and I. H. Suzuki, A study on multi-charged Xe ions formed through 3d hole states using a coincidence technique, J. Phys. B: At. Mol. Opt. Phys. **35**, 2799 (2002).

[32] V. Jonauskas, L. Partanen, S. Kučas, R. Karazija, M. Huttula, S. Aksela, and H. Aksela, Auger cascade satellites following 3d ionization in xenon, J. Phys. B: At. Mol. Opt. Phys. **36**, 4403 (2003).

[33] R. Guillemin, K. Jänkälä, B. C. De Miranda, T. Marin, L. Journel, T. Marchenko, O. Travnikova, G. Goldsztejn, I. Ismail, R. Püttner, D. Céolin, B. Lassalle-Kaiser, M. N. Piancastelli, and M. Simon, Interplay of complex decay processes after argon 1*s* ionization, Phys. Rev. A **97**, 013418 (2018).

[34] Y. Hikosaka, P. Lablanquie, F. Penent, T. Kaneyasu, E. Shigemasa, J. H. D. Eland, T. Aoto, and K. Ito, Double photoionization into double core-hole states in Xe, Phys. Rev. Lett. **98**, 183002 (2007).

[35] M. Mailhiot, K. Jänkälä, M. Huttula, M. Patanen, K. Bučar, M. Žitnik, D. Cubaynes, F. Holzmeier, R. Feifel, D. Céolin, L. Andric, R. Guillemin, I. Ismail, J. Palaudoux, F. Penent, and P. Lablanquie, Multielectron coincidence spectroscopy of the Ar^{2+} ($2p^{-2}$) double-core-hole decay, Phys. Rev. A **107**, 063108 (2023).

[36] Y. Hikosaka, P. Lablanquie, T. Kaneyasu, J. Adachi, H. Tanaka, I. H. Suzuki, M. Ishikawa, and T. Odagiri, Super-Coster-Kronig decay of Kr 3p core-hole states studied by multielectron coincidence spectroscopy, Phys. Rev. A **103**, 043119 (2021).

[37] J.-P. Rueff, J. M. Ablett, D. Céolin, D. Prieur, T. Moreno, V. Balédent, B. Lassalle-Kaiser, J. E. Rault, M. Simon, and A. Shukla, The GALAXIES beamline at the SOLEIL synchrotron: Inelastic X-ray scattering and photoelectron spectroscopy in the hard X-ray range, J. Synchrotron Radiat. **22**, 175 (2015).

[38] K. Chernenko, *et al.*, Performance and characterization of the FinEstBeAMS beamline at the MAX IV Laboratory, J. Synchrotron Radiat. **28**, 1620 (2021).

[39] D. Céolin, J. M. Ablett, D. Prieur, T. Moreno, J. P. Rueff, T. Marchenko, L. Journel, R. Guillemin, B. Pilette, T. Marin, and M. Simon, Hard x-ray photoelectron spectroscopy on the GALAXIES beamline at the SOLEIL synchrotron, J. Electron Spectrosc. Relat. Phenom. **190**, 188 (2013).

[40] O. F. Hagena, Condensation in free jets: Comparison of rare gases and metals, Z. Phys. D **4**, 291 (1987).

[41] U. Buck and R. Krohne, Cluster size determination from diffractive He atom scattering, J. Chem. Phys. **105**, 5408 (1996).

[42] X. Holzapfel, A. Schrodt, G. Hartmann, L. Marder, P. Schmidt, C. Ozga, P. Reiß, F. Wiegandt, A. Ehresmann, A. Hans, and A. Knie, Determination of mean cluster sizes by fluorescence detection upon site-specific photoexcitation, J. Phys. Chem. A **124**, 5352 (2020).

[43] R. Karnbach, M. Joppien, J. Stapelfeldt, J. Wörmer, and T. Möller, CLULU: An experimental setup for luminescence measurements on van der Waals clusters with synchrotron radiation, Rev. Sci. Instrum. **64**, 2838 (1993).

[44] M. Breinig, M. H. Chen, G. E. Ice, F. Parente, B. Crasemann, and G. S. Brown, Atomic inner-shell level energies determined by absorption spectrometry with synchrotron radiation, Phys. Rev. A **22**, 520 (1980).

[45] M. Mucke, M. Förstel, T. Lischke, T. Arion, A. M. Bradshaw, and U. Hergenhahn, Performance of a short "magnetic bottle" electron spectrometer, Rev. Sci. Instrum. **83**, 063106 (2012).

[46] P. Kruit and F. H. Read, Magnetic field paralleliser for 2π electron-spectrometer and electron-image magnifier, J. Phys. E **16**, 313 (1983).

[47] M. Cardona and L. Ley, *Photoemission in Solids I—General Principles* (Springer, Berlin, 1978), Vol. 1.

[48] M. Patanen, S. Benkoula, C. Nicolas, A. Goel, E. Antonsson, J. J. Neville, and C. Miron, Interatomic scattering in energy dependent photoelectron spectra of Ar clusters, J. Chem. Phys. **143**, 124306 (2015).

[49] P. Virtanen, *et al.*, SciPy 1.0: Fundamental algorithms for scientific computing in Python, Nat. Methods **17**, 261 (2020).

[50] R. Storn and K. Price, Differential evolution—A simple and efficient heuristic for global optimization over continuous spaces, J. Global Optim. **11**, 341 (1997).

[51] M. N. Piancastelli, K-shell double core-hole spectroscopy in molecules, Eur. Phys. J.: Spec. Top. **222**, 2035 (2013).

[52] M. Mucke, J. H. Eland, O. Takahashi, P. Linusson, D. Lebrun, K. Ueda, and R. Feifel, Formation and decay of core-orbital vacancies in the water molecule, Chem. Phys. Lett. **558**, 82 (2013).

[53] T. Mazza, *et al.*, Mapping resonance structures in transient core-ionized atoms, Phys. Rev. X **10**, 041056 (2020).

[54] I. Ismail, *et al.*, Alternative pathway to double-core-hole states, Phys. Rev. Lett. **131**, 253201 (2023).

[55] F. Trinter, L. Inhester, R. Püttner, S. Malerz, S. Thürmer, T. Marchenko, M. N. Piancastelli, M. Simon, B. Winter, and U. Hergenhahn, Radiationless decay spectrum of O 1s double core holes in liquid water, J. Chem. Phys. **160**, 194503 (2024).

[56] L. Asplund, P. Kelfve, B. Blomster, H. Siegbahn, and K. Siegbahn, Argon *KLL* and *KLM* Auger electron spectra, Phys. Scr. **16**, 268 (1977).

[57] R. Püttner, P. Holzhey, M. Hrast, M. Žitnik, G. Goldsztejn, T. Marchenko, R. Guillemin, L. Journel, D. Koulentianos, O. Travnikova, M. Zmerli, D. Céolin, Y. Azuma, S. Kosugi, A. F. Lago, M. N. Piancastelli, and M. Simon, Argon *KLL* Auger spectrum: Initial states, core-hole lifetimes, shake, and knock-down processes, Phys. Rev. A **102**, 052832 (2020).

[58] O. Björneholm, F. Federmann, F. Fössing, and T. Möller, Core level photelectron and x-ray absorption spectroscopy of free argon clusters: Size-dependent energy shifts and determination of surface atom coordination, Phys. Rev. Lett. **74**, 3017 (1995).

[59] M. Tchaplyguine, R. R. Marinho, M. Gisselbrecht, J. Schulz, N. Mårtensson, S. L. Sorensen, A. Naves de Brito, R. Feifel, G. Öhrwall, M. Lundwall, S. Svensson, and O. Björneholm, The size of neutral free clusters as manifested in the relative bulk-to-surface intensity in core level photoelectron spectroscopy, J. Chem. Phys. **120**, 345 (2004).

[60] L. O. Werme, T. Bergmark, and K. Siegbahn, The high resolution $L_{2,3}$ *MM* and $M_{4,5}$ *NN* Auger spectra from krypton and $M_{4,5}$ *NN* and $N_{4,5}$ *OO* Auger spectra from xenon, Phys. Scr. **6**, 141 (1972).

[61] C. Küstner-Wetekam, L. Marder, D. Bloß, C. Honisch, N. Kiefer, C. Richter, S. Rubik, R. Schaf, C. Zindel, M. Förstel, K. Gokhberg, A. Knie, U. Hergenhahn, A. Ehresmann, P. Kolorenč, and A. Hans, Experimental quantification of site-specific efficiency of interatomic Coulombic decay after inner shell ionization, Commun. Phys. **6**, 50 (2023).

[62] R. Sundaramoorthy, A. H. Weiss, S. L. Hulbert, and R. A. Bartynski, Direct evidence for dynamic broadening of the energy spectra associated with the later steps of an Auger cascade, Phys. Rev. Lett. **101**, 127601 (2008).

[63] M. Newville, R. Otten, A. Nelson, T. Stensitzki, A. Ingargiola, D. Allan, A. Fox, F. Carter, and M. Rawlik, LMFIT: Non-linear least-squares minimization and curve-fitting for Python, Zenodo (2025), https://zenodo.org/records/16175987.

[64] T. X. Carroll, J. D. Bozek, E. Kukk, V. Myrseth, L. J. Sæthre, and T. D. Thomas, Line shape and lifetime in argon 2p electron spectroscopy, J. Electron Spectrosc. Relat. Phenom. **120**, 67 (2001).

[65] R. Dupuy, F. Penent, B. Lutet-Toti, V. Duval, J. Palaudoux, and D. Céolin, Postcollision interaction in the liquid phase: The role of electron scattering, Phys. Rev. A **112**, 022824 (2025).